FEMs on Composite Meshes for Tuning Plasma Equilibria in Tokamaks

Holger Heumann, Francesca Rapetti, Xiao Song

FEMs on Composite Meshes for Tuning Plasma Equilibria in Tokamaks

Holger Heumann, Francesca Rapetti, Xiao Song

RESEARCH REPORT
N° 9129
December 2017
Project-Teams CASTOR

ISSN 0249-6399 ISRN INRIA/RR--9129--FR+ENG

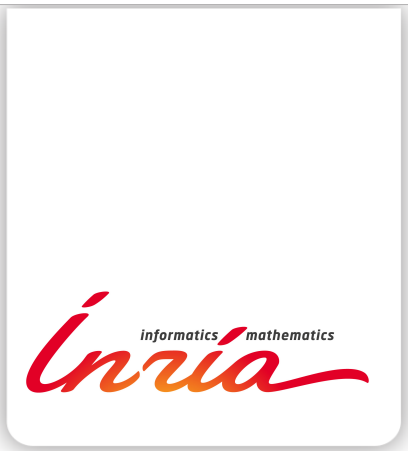

FEMs on Composite Meshes for Tuning Plasma Equilibria in Tokamaks

Holger Heumann, Francesca Rapetti, Xiao Song

Project-Teams CASTOR

Research Report n° 9129 — December 2017 — 16 pages

Abstract: We rely on a combination of different finite element methods on composite meshes, for the simulation of axisymmetric plasma equilibria in tokamaks. One mesh with Cartesian quadrilaterals covers the burning chamber and one mesh with triangles discretizes the region outside the chamber. The two meshes overlap in a narrow region around the chamber. This approach gives the flexibility to achieve easily and at low cost higher order regularity for the approximation of the flux function in the area that is covered by the plasma, while preserving accurate meshing of the geometric details in the exterior. The continuity of the numerical solution across the boundary of each subdomain is enforced by a mortar-like projection. We show that higher order regularity is very beneficial to improve computational tools for tokamak research.

Key-words: finite elements, plasma equilibrium, tokamak

RESEARCH CENTRE
SOPHIA ANTIPOLIS – MÉDITERRANÉE

2004 route des Lucioles - BP 93
06902 Sophia Antipolis Cedex

Des maillages composites pour la simulation des équilibres plasma dans les tokamaks

Résumé : Nous allons utiliser différentes méthodes d'éléments finis sur des maillages composite, pour la simulation des équilibres du plasma dans les tokamaks. Un maillage composé de rectangles avec des quadrilatérales cartésiennes couvre la chambre de combustion et une autre maillage des triangles discrétise la région à l'extérieur de la chambre. Les deux maillages se chevauchent dans une région étroite autour de la chambre. Cette approche a la flexibilité nécessaire pour réaliser facilement et à moindre coût une régularité plus élevé pour l'approximation du flux magnétique dans la zone couverte par le plasma, tout en préservant des détails géométriques à l'extérieur. La continuité de la solution numérique à travers la limite de chaque sous-domaine est imposée par une projection de type mortar. Nous montrons que la régularité d'ordre supérieur est très bénéfique pour affiner les outils de calcul qui sont utilisés en recherche pour mieux maitriser les experiments dans des tokamaks.

Mots-clés : éléments finis, équilibre du plasma, tokamak

Noname manuscript No.
(will be inserted by the editor)

FEMs on Composite Meshes for Tuning Plasma Equilibria in Tokamaks

Holger Heumann, Francesca Rapetti, Xiao Song

the date of receipt and acceptance should be inserted later

Abstract We rely on a combination of different finite element methods on composite meshes, for the simulation of axisymmetric plasma equilibria in tokamaks. One mesh with Cartesian quadrilaterals covers the burning chamber and one mesh with triangles discretizes the region outside the chamber. The two meshes overlap in a narrow region around the chamber. This approach gives the flexibility to achieve easily and at low cost higher order regularity for the approximation of the flux function in the area that is covered by the plasma, while preserving accurate meshing of the geometric details in the exterior. The continuity of the numerical solution across the boundary of each subdomain is enforced by a mortar-like projection. We show that higher order regularity is very beneficial to improve computational tools for tokamak research.

1 Introduction

The possibility of using composite meshes in finite element (FE) simulations of industrial problems is a recurrent topic [24,29,10,6,26]. Composite meshes are involved as soon as the global discretization of a PDE combines discretizations on local (overlapping or non-overlapping) subdomains, each suitably triangulated by non-matching grids. The reason for using composite meshes are various: fitting the geometry or the local smoothness of the solution, resolving multiple scales in regions with irregular data, using fast solvers on structured grids or a divide-and-conquer/domain decomposition approach to very large problems on parallel machines.

In the present case, we are looking for a simple and practical approach to introduce in certain parts of the computational domain FE functions that are not only continuous, but have also first order, second order or higher order continuous derivatives. In general it is very difficult to introduce FE spaces over simplicial unstructured meshes with such

Holger Heumann and Xiao Song
INRIA, CASTOR team, 2004 Route des Lucioles BP 93 06902 Sophia Antipolis, France, E-mail: Holger.Heumann@inria.fr; Xiao.Song@inria.fr

Francesca Rapetti
Dept. of Mathematics, Univ. de Nice, Parc Valrose, 06108 Nice cedex 02, France,
E-mail: Francesca.Rapetti@unice.fr

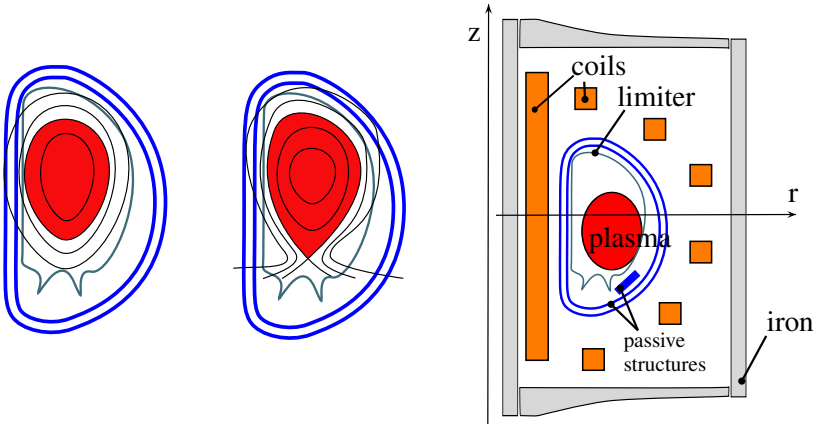

Fig. 1 Right: Geometric description of the tokamak in the poloidal plane. Left and middle: Sketch for characteristic plasma shapes. The plasma boundary touches the limiter (middle) or the plasma is enclosed by a flux line that goes through an X-point (right).

properties. On the other hand, if we work with Cartesian meshes this becomes very simple. It is sufficient to use tensor products of spline spaces with sufficiently high regularity. So, as it is naive to expect that technical devices can be entirely triangulated with Cartesian meshes, we introduce composite meshes involving Cartesian meshes in those subdomains where we want high regular FE representations and triangular unstructured meshes in those subdomains where we want conformity with the geometry.

The industrial application we consider concerns the free boundary plasma equilibrium in tokamaks for nuclear fusion [4], mathematically described by the force balance and Maxwell's equations in the eddy-current approximation. By symmetry considerations, the free boundary plasma equilibrium problem can be reduced to a scalar semi-linear elliptic one for the poloidal flux. As the magnetic field and the current density are tangential to the level sets of the poloidal flux, the precise calculation of the level set distribution for the poloidal flux is fundamental in tokamak science. Hence, it is important to have good approximations not only of the poloidal flux but also of its derivatives.

In Fig. 1 we show a sketch of the cross section of a tokamak. It contains the geometrical details such as coils, passive structures and the iron core, that need to be accurately resolved by a triangulation. A peculiarity of the free boundary plasma equilibrium problem is the unknown plasma domain, that is implicitly given as the domain that is bounded by the largest level set that it not intersected by the limiter. Depending on the combination of coil currents, the plasma either lies against the carbon tile covered wall of the vacuum vessel, the so-called limited configuration, or is fully detached from the wall thanks to the presence of a saddle point in the poloidal field (X-point) and the resulting separatrix that delimits the plasma. In the very early tokamak devices the plasma was always attached to the limiter, while later the focus shifted towards devices with so called divertors that allow to create plasmas that are completely detached from material. Particles that escape from the plasma may damage the surface of the divertor because they deposit their significant energy on a relatively small area leading to unacceptably high heat flux densities. To mitigate the heat flux impact several strategies are proposed. One of these strategies aims at the exploration of the so-called snowflake-like configuration.

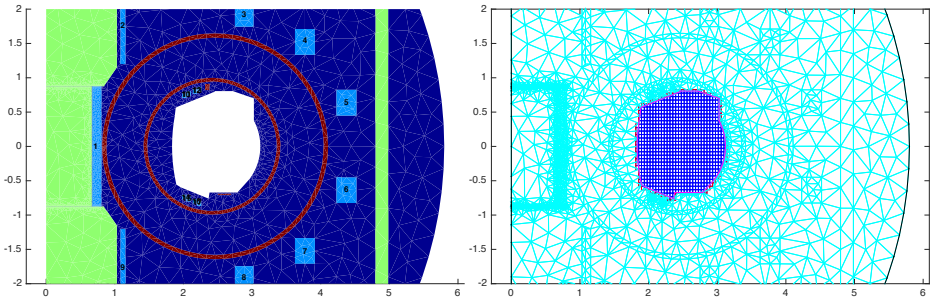

Fig. 2 Left: detail view for the WEST tokamak, with the iron core (green), the passive structures (red) and the various coils (light blue). Right: the composite meshes for the WEST tokamak.

A snowflake configuration is obtained when there is a point where not only the gradient of the poloidal flux vanishes but also its second order derivatives. This second condition implies that more than four contour lines meet in this point. The name 'snowflake' comes from the particular shape of this geometry. It thus results that the heat flux power may be diverted towards four sections of the chamber walls, thereby reducing the heat flux densities onto the divertor plates. The snowflake configuration was proposed by Ryutov *et al.* [27, 28].

In [17], we showed that the numerical calculation of free boundary plasma equilibria highly benefits from approximating the poloidal flux through some higher regular FE functions in the interior of the limiter. In the present paper we show, how the composite meshes and higher regular FE functions allow to single out such snowflake configurations. While FE methods on composite meshes are widely used in practice, their theoretical foundation is fairly limited in the literature. Therefore, we report here also extensive experimental convergence results that provide reassuring foundations for this application.

The outline is the following: In Sect. 2.1 we recall the classical mortar element method (MEM) for overlapping meshes in order to introduce, in the following Sect. 2.2, a modified method (MEM-M) that simplifies the implementation by avoiding integrals over cut elements. We then present experimental convergence results in Sect. 2.3. The Sect. 3 deals with the application of MEM to the free-boundary plasma equilibrium problem. We present the model (Sect. 3.5), the free-boundary equilibrium problem, and its role for the operation of tokamaks (Sect. 3.2). Next, in Sect. 3.3 and 3.4 we recall the Galerkin formulation of the model and the related optimal control problem. We explain, how Newton's method for the free-boundary equilibrium problem, can be easily extended to solve efficiently the corresponding optimal control problems. The paper ends with a case study for finding snowflake configurations.

2 FEMs on Composite Meshes

We present first the mortar element method with overlapping meshes. A complete convergence theory is available for this method, but has the drawback that it is based on integration over cut elements. We rather rely on a variant of the mortar element method that avoids working on cut elements.

2.1 The Mortar Element Method (MEM) with Overlapping Meshes

We consider the following Poisson problem for the unknown ψ in the bounded domain $\Omega \subset \mathbb{R}^n$ with boundary $\Gamma = \partial\Omega$:

$$-\nabla\cdot(K\nabla\psi) = f \quad \text{in } \Omega \quad \text{and} \quad \psi_{|\partial\Omega} = \psi_0 \quad \text{in } \Gamma\,, \tag{1}$$

where ∇ ($\nabla\cdot$) is the gradient (divergence) operator in $\mathbb{R}^n$ and $K \in \mathbb{R}$ positive. The right-hand side f and the Dirichlet data ψ_0 are given. Let $L^2(\Omega)$, be the functional space of measurable functions on Ω that are square integrable in Ω and $H^1(\Omega) = \{u \in L^2(\Omega),\, \nabla u \in L^2(\Omega)^2\}$ the Hilbert space endowed with the norm $\|u\|^2_{H^1(\Omega)} = \|u\|^2_\Omega + |u|^2_{H^1(\Omega)}$ where $|u|^2_{H^1(\Omega)} = \|\nabla u\|^2_\Omega$. Let $\Omega^{\text{in}} \subset \Omega$ be a subdomain with $\Omega^{\text{in}} \cap \Gamma = \emptyset$ and $\Omega^{\text{ex}} = \Omega \setminus \Omega^{\text{in}}$ the complement of Ω^{in} in Ω. Further, the boundary of Ω^{in}, $\gamma := \partial\Omega^{\text{in}}$, is the interface between Ω^{ex} and Ω^{in}. To formulate (7) as a variational problem in a domain decomposition framework, let us introduce the functional space

$$\mathscr{H}_g = \{(v,w) \in H^1(\Omega^{\text{ex}}) \times H^1(\Omega^{\text{in}}),\, v_{|\Gamma} = g,\, v_{|\gamma} = w_{|\gamma}\}.$$

Then, the weak formulation of (7) is: Find $(\psi^{\text{ex}}, \psi^{\text{in}}) \in \mathscr{H}_{\psi_0}$ s.t. for all $(v,w) \in \mathscr{H}_0$

$$\int_{\Omega^{\text{ex}}} K\nabla\psi^{\text{ex}}\cdot\nabla v\,\mathrm{d}\mathbf{x} + \int_{\Omega^{\text{in}}} K\nabla\psi^{\text{in}}\cdot\nabla w\,\mathrm{d}\mathbf{x} = \int_{\Omega^{\text{ex}}} f v\,\mathrm{d}\mathbf{x} + \int_{\Omega^{\text{in}}} f w\,\mathrm{d}\mathbf{x}. \tag{2}$$

We wish to introduce different types of meshes $\mathscr{T}^{\text{ex}}$ and $\mathscr{T}^{\text{in}}$ in the two subdomains Ω^{ex} and Ω^{in}. To achieve a maximum of flexibility we do not expect the meshes $\mathscr{T}^{\text{ex}}$ and $\mathscr{T}^{\text{in}}$ to be conforming with Ω^{ex} and Ω^{in}. More precisely, we denote by Ω^{ex}_h and Ω^{in}_h the domains covered by the mesh elements of $\mathscr{T}^{\text{ex}}$ and $\mathscr{T}^{\text{in}}$, respectively, and we only require that $\Omega^{\text{ex}} \subset \Omega^{\text{ex}}_h \subset \Omega$, $\Gamma \subset \partial\Omega^{\text{ex}}_h$ and $\Omega^{\text{in}} \subset \Omega^{\text{in}}_h \subset \Omega$. Hence the approximation of (2) enters into the framework of overlapping domain decomposition methods. Let $\gamma^{\text{ex}} = \partial\Omega^{\text{ex}}_h \setminus \Gamma$ and $\gamma^{\text{in}} = \partial\Omega^{\text{in}}_h$ be the two boundaries of Ω^{ex}_h and Ω^{in}_h in Ω that replace the interface γ. Then we introduce the space

$$\mathscr{V}_g = \{(v,w) \in \mathscr{V}^{\text{ex}} \times \mathscr{V}^{\text{in}},\, v_{|\Gamma} = \Pi^{\text{Dir}} g,\, v_{|\gamma^{\text{ex}}} = \Pi^{\text{ex}} w,\, w_{|\gamma^{\text{in}}} = \Pi^{\text{in}} v\}\,,$$

where $\mathscr{V}^{\text{ex}}$ and $\mathscr{V}^{\text{in}}$ are $H^1(\Omega^{\text{ex}}_h)$ and $H^1(\Omega^{\text{in}}_h)$ conforming FE spaces defined over $\mathscr{T}^{\text{ex}}$ and $\mathscr{T}^{\text{in}}$. The operators Π^{Dir}, Π^{ex} and Π^{in} are projections onto the Dirichlet trace spaces $\mathscr{V}_\Gamma = \text{tr}_{|\Gamma}\,\mathscr{V}^{\text{ex}}$, $\mathscr{V}^{\text{ex}}_\gamma := \text{tr}_{|\gamma^{\text{ex}}}\,\mathscr{V}^{\text{ex}}$ and $\mathscr{V}^{\text{in}}_\gamma := \text{tr}_{|\gamma^{\text{in}}}\,\mathscr{V}^{\text{in}}$. The MEM$_{s,t}$ with overlapping domains [20,5,1] applied to (2) reads: Find $(\psi^{\text{ex}}, \psi^{\text{in}}) \in \mathscr{V}_{\psi_0}$ such that

$$\mathsf{a}^{\text{ex}}_s(\psi^{\text{ex}}, v) + \mathsf{a}^{\text{in}}_t(\psi^{\text{in}}, w) = \ell^{\text{ex}}_s(f,v) + \ell^{\text{in}}_t(f,w) \quad \forall (v,w) \in \mathscr{V}_0\,, \tag{3}$$

where

$$\mathsf{a}^{\text{M}}_s(\psi, v) := \int_{\Omega^{\text{M}}_h} K\nabla\psi\cdot\nabla v\,\mathrm{d}\mathbf{x} - \int_{\Omega^{\text{ex}}_h\cap\Omega^{\text{in}}_h} sK\nabla\psi\cdot\nabla v\,\mathrm{d}\mathbf{x},$$
$$\ell^{\text{M}}_s(f,v) := \int_{\Omega^{\text{M}}_h} f v\,\mathrm{d}\mathbf{x} - \int_{\Omega^{\text{ex}}_h\cap\Omega^{\text{in}}_h} s f\, v\,\mathrm{d}\mathbf{x},$$

for M = ex and M = in. Optimal convergence results are available when $s+t=1$ and Π^{ex}, Π^{in}, are the L^2 projections onto $\text{tr}_{|\gamma^{\text{ex}}}\,\mathscr{V}^{\text{ex}}$, $\text{tr}_{|\gamma^{\text{in}}}\,\mathscr{V}^{\text{in}}$, respectively [5,1]. However, two very restrictive disadvantages occur with the formulation (3):

1. The assembling of the stiffness matrices associated to $\mathsf{a}_s^{\mathrm{ex}}(\cdot,\cdot)$ and $\mathsf{a}_t^{\mathrm{in}}(\cdot,\cdot)$ involves products of basis functions defined on different meshes. Similarly, the assembling of the load vectors corresponding to $\ell_s^{\mathrm{ex}}(f,\cdot)$ and $\ell_t^{\mathrm{in}}(f,\cdot)$ involves integration over intersections of elements from different meshes.
2. The stability of $\mathrm{MEM}_{s,t}$ requires the projections Π^{ex} and Π^{in} to be stable in $H^{\frac{1}{2}}$. The obvious choice of L^2 projections involves again surface integrals of products of basis functions defined on different meshes.

In the following section we will introduce two mortar-like mappings different from the standard L^2 projection, that allow to choose $s=t=0$ in (3) and hence avoid the assembling of the stiffness matrix for basis functions on two different meshes.

2.2 A Modified Mortar Mapping (MEM-M)

We recall that the FE spaces $\mathscr{V}^{\mathrm{ex}}$ and $\mathscr{V}^{\mathrm{in}}$ can be represented as direct sums $\mathscr{V}^{\mathrm{ex}} = \mathscr{V}_\circ^{\mathrm{ex}} \oplus E\mathscr{V}_\gamma^{\mathrm{ex}}$ and $\mathscr{V}^{\mathrm{in}} = \mathscr{V}_\circ^{\mathrm{in}} \oplus E\mathscr{V}_\gamma^{\mathrm{in}}$ where $\mathscr{V}_\gamma^{\mathrm{ex}} = \mathrm{tr}_{|\gamma^{\mathrm{ex}}}\mathscr{V}^{\mathrm{ex}}$ and $\mathscr{V}_\gamma^{\mathrm{in}} = \mathrm{tr}_{|\gamma^{\mathrm{in}}}\mathscr{V}^{\mathrm{in}}$ are the earlier introduced trace spaces of $\mathscr{V}^{\mathrm{ex}}$ and $\mathscr{V}^{\mathrm{in}}$. where E is the trivial extension operator. Let us introduce two mappings $\Pi_f^{\mathrm{ex}}\psi^{\mathrm{in}}$ for $\psi^{\mathrm{in}} = \psi_\circ^{\mathrm{in}} + \psi_\gamma^{\mathrm{in}}$, with $\psi_\circ^{\mathrm{in}} \in \mathscr{V}_\circ^{\mathrm{in}}$, $\psi_\gamma^{\mathrm{in}} \in \mathscr{V}_\gamma^{\mathrm{in}}$ and $\Pi_f^{\mathrm{in}}\psi^{\mathrm{ex}}$ for $\psi^{\mathrm{ex}} = \psi_\circ^{\mathrm{ex}} + \psi_\gamma^{\mathrm{ex}}$, with $\psi_\circ^{\mathrm{ex}} \in \mathscr{V}_\circ^{\mathrm{ex}}$, $\psi_\gamma^{\mathrm{ex}} \in \mathscr{V}_\gamma^{\mathrm{ex}}$. The mapping Π_f^{ex} is defined as:

$$\Pi_f^{\mathrm{ex}}\psi^{\mathrm{in}} := \Pi^{\mathrm{ex}}(\psi_\gamma^{\mathrm{in}} + \Psi^{\mathrm{in}}),\ \text{with}\ \mathsf{a}_0^{\mathrm{in}}(\Psi^{\mathrm{in}},w) = \ell_0^{\mathrm{in}}(f,w) - \mathsf{a}_0^{\mathrm{in}}(\psi_\gamma^{\mathrm{in}},w) \quad \forall w \in \mathscr{V}_\circ^{\mathrm{in}},$$

where Π^{ex} is either the L^2-projection or standard nodal interpolation operator onto $\mathscr{V}_\gamma^{\mathrm{ex}}$. The mapping Π_f^{in} is defined analogously. We then introduce the space

$$\mathscr{V}_{g,f} = \{(v,w) \in \mathscr{V}^{\mathrm{ex}} \times \mathscr{V}^{\mathrm{in}},\ v_{|\Gamma} = \Pi^{\mathrm{Dir}}g,\ v_{|\gamma^{\mathrm{ex}}} = \Pi_f^{\mathrm{ex}}w,\ w_{|\gamma^{\mathrm{in}}} = \Pi_f^{\mathrm{in}}v\},$$

and obtain the following modified version of the MEM for overlapping meshes: Find $(\psi^{\mathrm{ex}},\psi^{\mathrm{in}}) \in \mathscr{V}_{\psi_0,f}$ such that

$$\mathsf{a}_0^{\mathrm{ex}}(\psi^{\mathrm{ex}},v) + \mathsf{a}_0^{\mathrm{in}}(\psi^{\mathrm{in}},w) = \ell_0^{\mathrm{ex}}(f,v) + \ell_0^{\mathrm{in}}(f,w) \quad \forall (v,w) \in \mathscr{V}_{0,0}, \tag{4}$$

A similar approach with the lowest order FE spaces in the non-destructive testing context has been adopted in [7,8]. The auxiliary variable Ψ^{in} is equal to $\psi_\circ^{\mathrm{in}}$, since we have both

$$\mathsf{a}_0^{\mathrm{in}}(\Psi^{\mathrm{in}},w) + \mathsf{a}_0^{\mathrm{in}}(\psi_\gamma^{\mathrm{in}},w) = \ell_0^{\mathrm{in}}(f,w) \quad \forall w \in \mathscr{V}_\circ^{\mathrm{in}},$$

and

$$\mathsf{a}_0^{\mathrm{in}}(\psi_\circ^{\mathrm{in}},w) + \mathsf{a}_0^{\mathrm{in}}(\psi_\gamma^{\mathrm{in}},w) = \ell_0^{\mathrm{in}}(f,w) \quad \forall w \in \mathscr{V}_\circ^{\mathrm{in}}.$$

Likewise the auxiliary variable Ψ^{ex} is equal to $\psi_\circ^{\mathrm{ex}}$. Hence it is easy to see that (4) is equivalent to the following formulation. Find $(\psi^{\mathrm{ex}},\psi^{\mathrm{in}}) \in \mathscr{V}^{\mathrm{ex}} \times \mathscr{V}^{\mathrm{in}}$, $\psi_{|\Gamma}^{\mathrm{ex}} = \Pi^{\mathrm{Dir}}g$ such that:

$$\begin{aligned} &\mathsf{a}_0^{\mathrm{ex}}(\psi^{\mathrm{ex}},v) + \mathsf{a}_0^{\mathrm{in}}(\psi^{\mathrm{in}},w) = \ell_0^{\mathrm{ex}}(f,v) + \ell_0^{\mathrm{in}}(f,w) \quad \forall (v,w) \in \mathscr{V}_\circ^{\mathrm{ex}} \times \mathscr{V}_\circ^{\mathrm{in}}, v_{|\Gamma=0} \\ &\psi_{|\gamma^{\mathrm{ex}}}^{\mathrm{ex}} = \Pi^{\mathrm{ex}}\psi^{\mathrm{in}} \qquad \psi_{|\gamma^{\mathrm{in}}}^{\mathrm{in}} = \Pi^{\mathrm{in}}\psi^{\mathrm{ex}}, \end{aligned} \tag{5}$$

which corresponds to the numerical zoom formulation in [16]. When Π^{ex} and Π^{in} are interpolation operators and $\mathscr{V}^{\mathrm{ex}}$ and $\mathscr{V}^{\mathrm{in}}$ are lowest order Lagrangian FE spaces we can recall an optimal convergence result from [21, Theorem 1] for the error in the L^∞-norm, under the assumption that discrete maximums principles and a certain monotonicity condition hold.

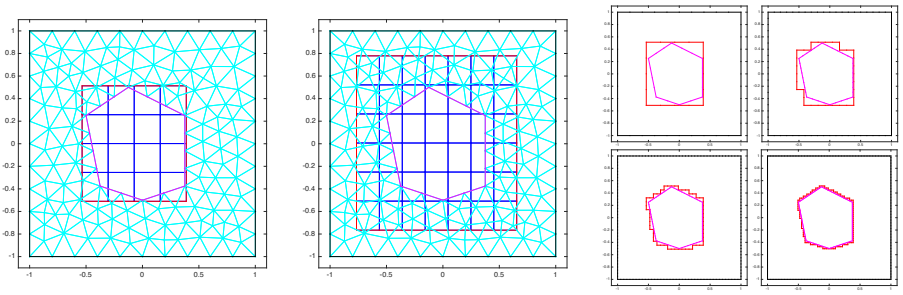

Fig. 3 Left and Center: Sketch of the two different settings. We may choose Ω_h^{in} to have a minimal overlap with Ω_h^{ex} (left), that is γ^{ex} is contained in the layer of elements of $\mathscr{T}^{\text{in}}$ which define γ^{in}. Otherwise, we say that Ω_h^{in} has a large overlap with Ω_h^{ex} (center). Right: Adaptive definition of γ^{in} in the case of minimal overlap between Ω_h^{in} and Ω_h^{ex}. Note that, γ^{ex} (magenta) remains fixed, while γ^{in} (red) changes due to the refinements in Ω_h^{in}. The interior edges of elements of $\mathscr{T}^{\text{ex}}$ and $\mathscr{T}^{\text{in}}$ are omitted for clearness.

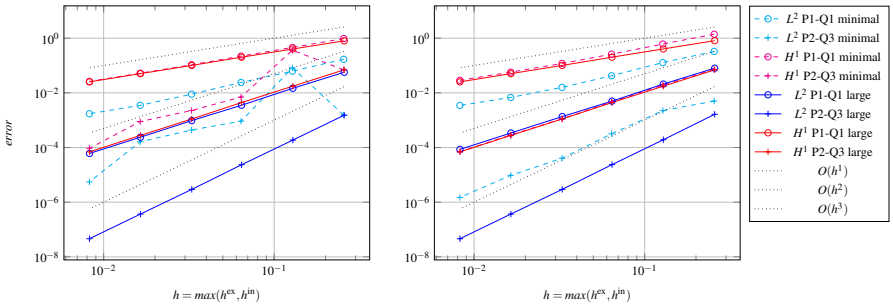

Fig. 4 Convergence in L^2 and H^1 of the scheme MEM-M using L^2-projection (left) or nodal interpolation (right).

2.3 Experimental Convergence Estimates

For the numerical experiments, we consider a rectangular domain $\Omega = [-1,1]^2$ and define Ω^{in} as the polygon with vertices $(-0.125, 0.5)$, $(0.375, 0.25)$, $(0.375, -0.375)$, $(0, -0.5)$, $(-0.375, -0.375)$, and $(-0.5, 0.25)$. The meshes $\mathscr{T}^{\text{in}}$ and $\mathscr{T}^{\text{ex}}$ for the interior and exterior domain will be a Cartesian mesh and a triangular mesh. For simplicity we prefer to take $\Omega_h^{\text{ex}} = \Omega^{\text{ex}} = \Omega \setminus \Omega^{\text{in}}$. For the numerical test, we take $K = 1$ and choose the data $f(x,y)$ and ψ_0 such that $\psi(x,y) = \cos(\pi x)\sin(\pi y)$ is the solution of (7). If h_{ex} (h_{in}) is the maximal diameter of elements in $\mathscr{T}^{\text{ex}}$ ($\mathscr{T}^{\text{in}}$), and p_{ex} (p_{in}) the local polynomial degree of the FE spaces $\mathscr{V}^{\text{ex}}$ ($\mathscr{V}^{\text{in}}$), one has optimal convergence if, for a smooth solution, the approximation error in the $H^1(\Omega_h^{\text{ex}})$ and $H^1(\Omega_h^{\text{in}})$-norms behaves as $O(h^{p-1})$, with $h = \max(h_{\text{ex}}, h_{\text{in}})$ and $p = \min(p_{\text{ex}}, p_{\text{in}})$ (in $L^2(\Omega_h^{\text{ex}})$ and $L^2(\Omega_h^{\text{in}})$-norms one dares to obtain $O(h^p)$). To keep the presentation as clear as possible we show in the following figures always the maximum between the error in Ω_h^{ex} and that in Ω_h^{in}.

We consider two different pairings of FE spaces $\mathscr{V}^{\text{ex}}$-$\mathscr{V}^{\text{in}}$. The first denoted with P1-Q1 uses lowest order linear FEs over $\mathscr{T}^{\text{ex}}$ and lowest order bilinear FEs over $\mathscr{T}^{\text{in}}$. The second pair, denoted with P2-Q3 uses quadratic FEs over $\mathscr{T}^{\text{ex}}$ and bicubic FEs over $\mathscr{T}^{\text{in}}$. The elements of P2-Q3 are not only continuous on Ω_h^{in} and Ω_h^{ex} but have also continuous gradients on Ω_h^{in}.

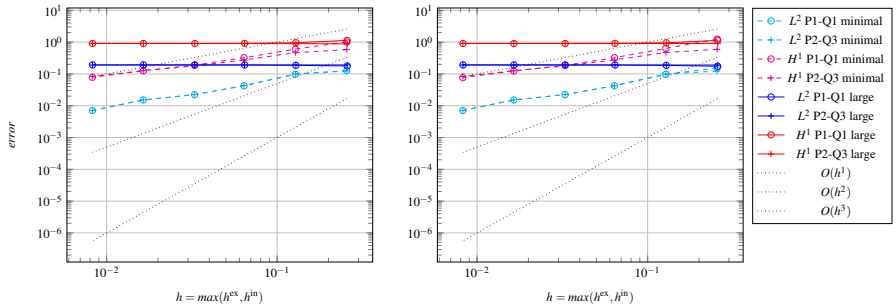

Fig. 5 Convergence in L^2 and H^1 of the scheme $\text{MEM}_{0,0}$ using L^2-projection (left) or nodal interpolation (right).

We focus on the overlapping MEM-M (4) which uses the modified mortar mappings and is equivalent to (5). We also analyse the influence on the error curves of using either L^2 projections or interpolation to realize the gluing across γ^{ex} and γ^{in} for the MEM-M. We start with the case where Ω_h^{in} has minimal overlap with Ω_h^{ex} (see Fig. 3, left). Thus γ^{in} is adapted with the refinements in Ω_h^{in} as shown in Fig. 3. Convergence results with MEM-M are presented in Fig. 4. The convergence rate with MEM-M is optimal for the error in the H^1-norm. The results look slightly better if we apply the interpolation instead of the L^2 projection in the definition of the mortar mapping.

Next, we study the convergence rates for MEM-M when Ω_h^{in} has a large overlap with Ω_h^{ex} (see Fig. 3, right). Note that both γ^{ex} and γ^{in} remain fixed during the refinements in Ω_h^{in}. Once again, the MEM-M yields optimal convergence rate in the H^1 norm (see Fig. 4). Moreover in the case of larger overlap we observe even optimal convergence in the L^2-norm. There is no qualitative difference between MEM-M based on the L^2-projection or on the interpolation. More detailed numerical tests of the MEM-M can be found in [31].

With the classical overlapping $\text{MEM}_{s,t}$ (3) with the parameters s and t set to zero ($\text{MEM}_{0,0}$), the convergence rates in the H^1 and L^2 norms are not optimal in the case of minimal overlap between Ω_h^{in} and Ω_h^{ex} (see Fig. 5). The $\text{MEM}_{0,0}$ does not yield convergence in the case of a large overlap between Ω_h^{in} and Ω_h^{ex}.

We highlight that, to our knowledge, there is no theory yet available, that justifies rigorously our experimental results for MEM-M. Only for lowest order Lagrangian elements we have a convergence assertion in L^∞ [21, Theorem 1]. Our experimental results for $\text{MEM}_{0,0}$ are not very surprising. All available convergence assertions assume $s+t=1$, which leads to the cumbersome integration over cut elements, that we prefer to avoid.

3 Composite Meshes for Tuning Plasma Equilibria

The essential equations for describing plasma equilibrium in a tokamak are force balance, the solenoidal condition and Ampère's law that read respectively

$$\operatorname{grad} p = \mathbf{J} \times \mathbf{B}, \qquad \operatorname{div} \mathbf{B} = 0, \qquad \operatorname{curl} \frac{1}{\mu} \mathbf{B} = \mathbf{J}, \tag{6}$$

where p is the plasma kinetic pressure, $\mathbf{B}$ is the magnetic induction, $\mathbf{J}$ is the current density and μ the magnetic permeability. The magnetodydrodymic equilibrium (6) is a fundamental concept for nuclear fusion and we refer to standard text books, e.g. [11], [4], [32], [12],

[13] and [19] for the details. Nevertheless, to keep this contribution concise, we give in the subsequent section a brief introduction following the lines of [17, Section 2].

3.1 The Free-Boundary Plasma Equilibrium Problem

Tokamaks are predominantly axial symmetric devices, hence it is convenient to formulate (6) in a cylindrical coordinate system (r,φ,z) in order to consider only a section at $\varphi =$ constant of the tokamak, generally referred to as *poloidal section*. $x = r\cos\varphi$ and $y = r\sin\varphi$. Working in a poloidal section, the scalar field p does not depend on the angle φ, thus ∇p belongs to the poloidal (r,z)-plane. We introduce $\mathbb{H} = [0,\infty]\times[-\infty,\infty]$, the positive half plane, to denote the poloidal plane that contains the tokamak centered at the origin. The classical primal unknowns for toroidal plasma equilibria described by (6) are the *poloidal magnetic flux* $\psi = \psi(r,z)$, the pressure p and the *diamagnetic function* f. The poloidal magnetic flux $\psi := r\mathbf{A}\cdot\mathbf{e}_\varphi$ is the scaled toroidal component (φ-component) of the magnetic vector potential $\mathbf{A}$, such that $\mathbf{B} = \operatorname{curl}\mathbf{A}$, and $\mathbf{e}_\varphi$ the unit vector for the φ coordinate. The diamagnetic function $f = r\mathbf{B}\cdot\mathbf{e}_\varphi$ is the scaled toroidal component of the magnetic field $\mathbf{B}$. It can be shown that both the pressure p and the diamagnetic function f are constant on ψ-isolines, i.e. $p = p(\psi)$ and $f = f(\psi)$.

Force balance, the solenoidal condition and Ampère's law in (6) yield, in axisymmetric configuration, the following set of equations for the flux $\psi(r,z)$:

$$\begin{aligned} -\nabla\cdot\left(\tfrac{1}{\mu[\psi]r}\nabla\psi\right) &= \begin{cases} rp'(\psi)+\frac{1}{\mu_0 r}ff'(\psi) & \text{in } \mathscr{P}(\psi);\\ I_i/|\mathscr{C}_i| & \text{in } \mathscr{C}_i;\\ j_{\mathscr{S}} & \text{in } \mathscr{S};\\ 0 & \text{elsewhere in } \mathbb{H}, \end{cases} \\ \psi(0,z) = 0; \qquad & \lim_{\|(r,z)\|\to+\infty}\psi(r,z) = 0; \end{aligned} \tag{7}$$

where ∇ is the gradient in the half plane $\mathbb{H}$, I_i is the total current (in At, Ampère turns) in the ith coil $\mathscr{C}_i \subset \mathbb{H}$ and μ is a functional of ψ that reads

$$\mu[\psi] = \begin{cases} \mu_{\mathrm{Fe}}(\frac{|\nabla\psi|^2}{r^2}) & \text{in } \mathscr{F}\\ \mu_0 & \text{elsewhere}, \end{cases} \tag{8}$$

with μ_0 the constant magnetic permeability of vacuum and μ_{Fe} the non-linear magnetic permeability of iron. $\mathscr{S}$ is the domain of axisymmetric passive structures where a current density $j_{\mathscr{S}}$ is prescribed. The plasma domain $\mathscr{P}(\psi)$ is an unknown, which depends non-linearly on the magnetic flux ψ: $\mathscr{P}(\psi)$ is a functional of the poloidal flux ψ. The different characteristic shapes of $\mathscr{P}(\psi)$ are illustrated in Figure 1: the boundary of $\mathscr{P}(\psi)$ either touches the boundary of $\mathscr{L}$ (limiter configuration) or the boundary contains one or more saddle points of ψ (divertor configuration). The saddle points of ψ, denoted by $(r_{\mathrm{X}},z_{\mathrm{X}})$=$(r_{\mathrm{X}}(\psi),z_{\mathrm{X}}(\psi))$, are called X-points of ψ. The plasma domain $\mathscr{P}(\psi)$ is the largest subdomain of $\mathscr{L}$ bounded by a closed ψ-isoline in $\mathscr{L}$ and containing the magnetic axis $(r_{\max},z_{\max})$. The magnetic axis is the point $(r_{\max},z_{\max}) = (r_{\max}(\psi),z_{\max}(\psi))$, where ψ has its global maximum in $\mathscr{L}$. For convenience, we introduce also the coordinates $(r_{\mathrm{bdp}},z_{\mathrm{bdp}}) = (r_{\mathrm{bdp}}(\psi),z_{\mathrm{bdp}}(\psi))$ of the point that determines the plasma boundary. Note that $(r_{\mathrm{bdp}},z_{\mathrm{bdp}})$ is either an X-point of ψ or the contact point with the limiter $\partial\mathscr{L}$. The Figure 6 presents the actual geometric setting of 3 different tokamaks showing the big variety of designs.

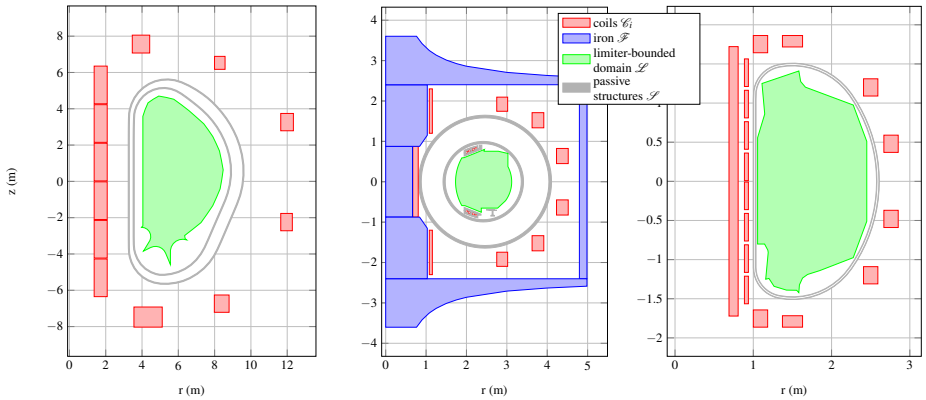

Fig. 6 The poloidal section of the tokamaks ITER (left), WEST (middle) and HL-2M (right). ITER, the International Thermonuclear Experimental Reactor, is currently build in Cadarache, France and planned to be operational in 2015. WEST, the Tungsten (W) Environment in Steady-state Tokamak, is the remodeled Tore Supra tokamak of the CEA, also located in Cadarache. Tora Supra was operational from 1988-2010 and experiments with WEST started in 2017. HL-2M is a modification of HL-2A, a tokamak in Chengdu, China operational since 2001.

The equation (7) in the plasma domain is the celebrated *Grad-Shafranov-Schlüter* equation [14,30,22]. The domain of p' and $f\,f'$ is the interval $[\psi_{\text{bdp}}, \psi_{\text{max}}]$ with the scalar values ψ_{max} and ψ_{bdp} being the flux values at the *magnetic axis* and at the boundary of the plasma:

$$\begin{aligned} \psi_{\text{max}}[\psi] &:= \psi(r_{\text{max}}[\psi], z_{\text{max}}[\psi])\,, \\ \psi_{\text{bdp}}[\psi] &:= \psi(r_{\text{bdp}}[\psi], z_{\text{bdp}}[\psi])\,. \end{aligned} \tag{9}$$

The two functions p' and $f\,f'$ and the currents I_i in the coils are not determined by the model (7) and have to be supplied as data. Since the domain of p' and $f\,f'$ depends on the poloidal flux itself, it is more practical to supply these profiles as functions of the normalized poloidal flux $\psi_{\text{N}}(r,z)$:

$$\psi_{\text{N}}(r,z) = \frac{\psi(r,z) - \psi_{\text{max}}[\psi]}{\psi_{\text{bdp}}[\psi] - \psi_{\text{max}}[\psi]}\,. \tag{10}$$

These two functions, subsequently termed $S_{p'}$ and $S_{ff'}$, have, independently of ψ, a fixed domain $[0,1]$. They are usually given as piecewise polynomial functions. Another frequent a priori model is

$$S_{p'}(\psi) = \lambda\,\frac{\beta}{r_0}(1-\psi_{\text{N}}^{\alpha})^{\gamma}, \quad S_{ff'}(\psi) = \lambda(1-\beta)\mu_0 r_0(1-\psi_{\text{N}}^{\alpha})^{\gamma}, \tag{11}$$

with r_0 the major radius (in meters) of the vacuum chamber and $\alpha,\beta,\gamma \in \mathbb{R}$ given parameters. We refer to [23] for a physical interpretation of these parameters. The parameter β is related to the poloidal beta [4, p. 15], whereas α and γ describe the peakage of the current profile, λ is a scaling parameter related to the total plasma current.

3.2 The Plasma Equilibrium and Tokamak Experiments

Computing plasma equilibria, the solutions to (7), is a central topic in tokamak fusion science. This is essential for simulations with elaborated high-dimensional magnetohydrodynamic (MHD) models but also for experimenters that need to control real tokamak reactors.

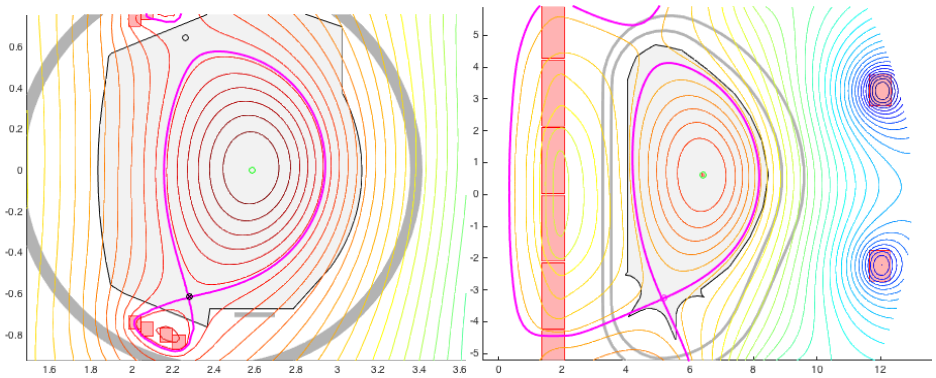

Fig. 7 Contour lines of the magnetic flux ψ for two different cases: WEST (left) and ITER (right). The location $(r_{\max}(\psi), z_{\max}(\psi))$ of the maximum of ψ is indicated with a green circle. The location (r_X, z_X) of the discrete saddle points of ψ is indicated by black circles. The magenta line indicates the contour line that contains the plasma boundary.

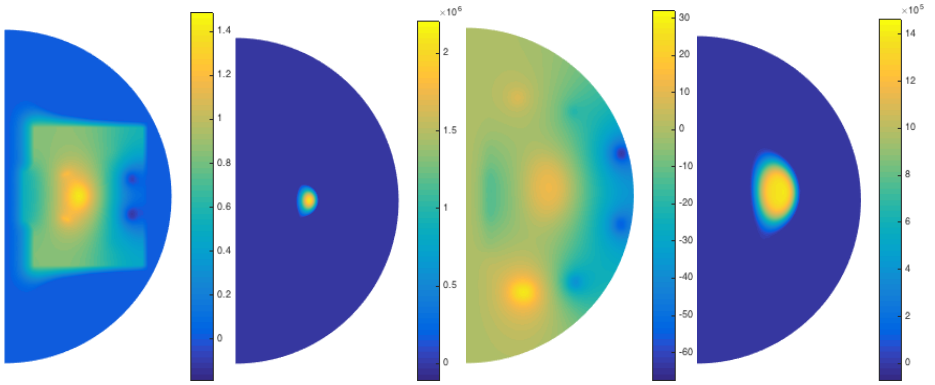

Fig. 8 Pseudo-color plot of the magnetic flux ψ and the plasma current density for two different cases: WEST (left) and ITER (right).

They need to compute a huge amount of equilibria to set up discharge scenarios, to study breakdowns and disruptions, or to design the layout of new machines. The computational challenges for numerical codes for such free-boundary equilibrium problems are a problem setting in an unbounded domain with non-linearities due the current density profile in the unknown plasma domain and the non-linear magnetic permeability if the reactor has ferromagnetic structures. Devising stable iterative schemes is known to be very tricky [25], in particular for computing physical unstable equilibria. The combination of Galerkin methods and Newton-type iterations that were first introduced in [3] are among the most successful approaches to such type of free-boundary problems. Computing derivatives of the plasma domain has similarities with shape calculus. We refer to [18] for details and the latest improvements and extensions of this approach.

In Figures 7, 8 and 9 we show a couple of representative examples for such equilibrium calculations. At this point, all the calculations are based on a standard Galerkin method with lowest order Lagrangian finite elements as described in [3] or [18].

In order to prepare experiments on each machine, it is a routine almost daily work, to compute not only the magnetic flux for a certain given set of coil currents, but also to

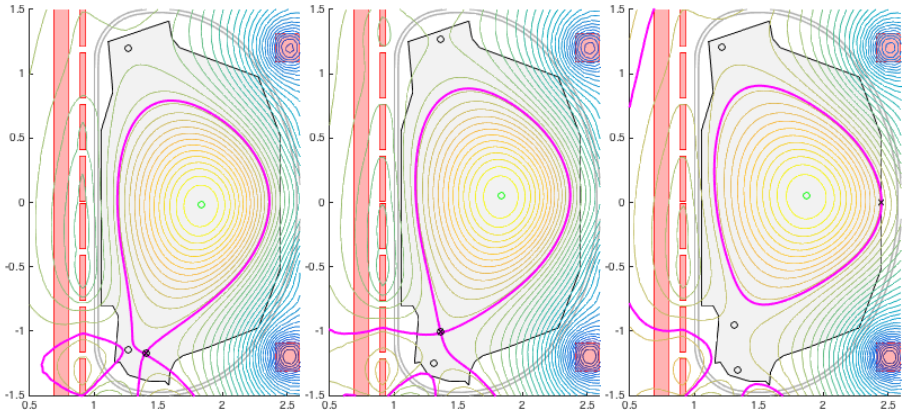

Fig. 9 Contour lines of the magnetic flux ψ for three different different configuration of HL-2M. The location $(r_{\max}(\psi), z_{\max}(\psi))$ of the maximum of ψ is indicated with a green circle. The location (r_X, z_X) of the discrete saddle points of ψ is indicated by black circles. The magenta line indicates the contour line that contains the plasma boundary.

determine coil currents that create a plasma equilibrium with certain desired properties. Such properties can be for example the shape of the plasma domain, the position of the X-point or the distribution of the plasma current density. It is very convenient to formulate such tasks as inverse or optimal control problem in introducing objective functionals that encode the design goals. A common choice would be the quadratic functional

$$K(\psi) = \sum_{i=1}^{N_{\text{desi}}} \big(\psi(r_i, z_i, t) - \psi(r_0, z_0, t)\big)^2,$$

that would help to find an plasma equilibrium that has constant ψ values on $N_{\text{desi}} + 1$ given points (r_i, z_i). However, from the definition of the equilibrium problem it is clear that the stationary points of the magnetic flux ψ have a very important role and it would be very beneficial to formulate objective functionals for these stationary points. Moreover, the location of the X-point has a big influence, where the extremely hot impurities released from the plasma core hit the walls of the reactor. Very recently it was discovered that the so-called snowflake configuration, with degenerated X-points or with many X-points close nearby (see Figure 9) can have very positive effects for the heat load mitigation, and hence, engineers are getting interested to prepare tokamak scenarios with such configurations.

However, with the current Galerkin approaches it is not so obvious how to formulate the objective functionals for such tasks. The gradients or Hessians of the Galerkin approximation of ψ are non-smooth across element boundaries. Point evaluations of these gradients and Hessians are not well defined. Therefor, we prefer to work with higher order regular Galerkin methods. As this is easy with Cartesian meshes, we are interested in combining Cartesian meshes covering the burning chamber with triangle meshes covering the remaining parts of the computational domain.

3.3 Galerkin Formulation

To adapt to the notation from section 2.2 we introduce $\mathbf{x} := (x_r, x_z) := (r, z)$. Next, we choose a semi-circle Γ of radius $\rho_\Gamma > 0$ surrounding the iron domain $\mathscr{F}$ and the coil domains $\mathscr{C}_i$.

Our computational domain $\Omega \subset \mathbb{H}$ is the half circle domain with the boundary $\partial\Omega = \Gamma \cup \Gamma_0$, where $\Gamma_0 := \{(0,x_z),\, -\rho_\Gamma \le x_z \le \rho_\Gamma\}$. The exterior domain Ω^{ex} that will be covered by a triangular mesh is the complement of the limiter-bounded domain $\mathscr{L}$ in Ω: $\Omega^{\text{ex}} = \Omega \setminus \mathscr{L}$. The interior domain Ω^{in} is the limiter-bounded domain $\mathscr{L}$ (see Figures 6 and 3). We arrive at the following MEM-M Galerkin formulation of the non-linear plasma equilibrium problem: Find $(\psi^{\text{ex}}, \psi^{\text{in}}) \in \mathscr{V}^{\text{ex}} \times \mathscr{V}^{\text{in}}$, $\psi^{\text{ex}}_{|\Gamma_0} = 0$ such that:

$$
\begin{aligned}
&\int_{\Omega_h^{\text{ex}}} \frac{\nabla\psi^{\text{ex}}(\mathbf{x})\cdot\nabla v(\mathbf{x})}{\mu[\psi^{\text{ex}}]x_r}\mathrm{d}\mathbf{x} + c(\psi^{\text{ex}}, v) - \sum_i \int_{\mathscr{C}_i} \frac{I_i}{|\mathscr{C}_i|} v(\mathbf{x})\mathrm{d}\mathbf{x} = 0 && \forall v \in \mathscr{V}_\circ^{\text{ex}}, v_{|\Gamma_0} = 0\\
&\int_{\Omega_h^{\text{in}}} \frac{\nabla\psi^{\text{in}}(\mathbf{x})\cdot\nabla w(\mathbf{x})}{\mu_0 x_r}\mathrm{d}\mathbf{x} - \int_{\mathscr{P}(\psi^{\text{in}})} \left(x_r S_{p'}(\psi^{\text{in}}(\mathbf{x})) + \frac{S_{ff'}(\psi^{\text{in}}(\mathbf{x}))}{\mu_0 x_r}\right) w(\mathbf{x})\mathrm{d}\mathbf{x} = 0 && \forall w \in \mathscr{V}_\circ^{\text{in}}\\
&\int_{\gamma^{\text{ex}}} \psi^{\text{ex}}(\mathbf{x})\lambda(\mathbf{x})\mathrm{d}\mathbf{s}(\mathbf{x}) - \int_{\gamma^{\text{ex}}} \Pi^{\text{ex}}\psi^{\text{in}}(\mathbf{x})\lambda(\mathbf{x})\mathrm{d}\mathbf{s}(\mathbf{x}) = 0 && \forall \lambda \in \mathscr{V}_\gamma^{\text{ex}}\\
&\int_{\gamma^{\text{in}}} \psi^{\text{in}}(\mathbf{x})\mu(\mathbf{x})\mathrm{d}\mathbf{s}(\mathbf{x}) - \int_{\gamma^{\text{in}}} \Pi^{\text{in}}\psi^{\text{ex}}(\mathbf{x})\mu(\mathbf{x})\mathrm{d}\mathbf{s}(\mathbf{x}) = 0 && \forall \mu \in \mathscr{V}_\gamma^{\text{in}}
\end{aligned}
\tag{12}
$$

The bilinear form $c(\cdot,\cdot)$ [2,15,9] takes into account the boundary conditions at infinity using Greens functions of the operator $-\nabla\cdot\left(\frac{1}{\mu x_r}\nabla\cdot\right)$. It is defined as follows

$$
\begin{aligned}
c(\psi,\xi) :=& \frac{1}{\mu_0}\int_\Gamma \psi(\mathbf{x})N(\mathbf{x})\xi(\mathbf{x})\mathrm{d}\mathbf{s}(\mathbf{x})\\
&+ \frac{1}{2\mu_0}\int_\Gamma\int_\Gamma (\psi(\mathbf{x})-\psi(\mathbf{y}))M(\mathbf{x},\mathbf{y})(\xi(\mathbf{x})-\xi(\mathbf{y}))ds(\mathbf{x})\mathrm{d}\mathbf{s}(\mathbf{y}),
\end{aligned}
\tag{13}
$$

with

$$
\begin{aligned}
M(\mathbf{x},\mathbf{y}) &= \frac{k(\mathbf{x},\mathbf{y})}{2\pi(x_r y_r)^{\frac{3}{2}}}\left(\frac{2-k(\mathbf{x},\mathbf{y})^2}{2-2k(\mathbf{x},\mathbf{y})^2}E(k(\mathbf{x},\mathbf{y})) - K(k(\mathbf{x},\mathbf{y}))\right),\\
N(\mathbf{x}) &= \frac{1}{x_r}\left(\frac{1}{\delta_+}+\frac{1}{\delta_-}-\frac{1}{\rho_\Gamma}\right) \text{ and } \delta_\pm = \sqrt{x_r^2+(\rho_\Gamma \pm x_z)^2},
\end{aligned}
$$

and

$$
k^2(\mathbf{x},\mathbf{y}) = \frac{4x_r y_r}{(x_r+y_r)^2+(x_z-y_z)^2}.
$$

$K(k)$ and $E(k)$ are the complete elliptic integrals of the first and second kind respectively.

We want to stress that the MEM-M Galerkin formulation (12) is a non-linear problem and we refer to [17] for details on the Newton-type methods for this problem.

3.4 The Inverse Problem

Combining the discretized free-boundary plasma equilibrium evolution (12) with discretized objective functionals we arrive at a finite dimensional optimal control formulation that is of the general form

$$
\min_{\mathbf{u},\mathbf{y}} K(\mathbf{y}) + R(\mathbf{u}) \quad \text{s.t.} \quad \mathbf{B}(\mathbf{y},\mathbf{u}) = 0\,. \tag{14}
$$

The state variable $\mathbf{y}$ contains the unknowns of the poloidal flux. The components of the control variable $\mathbf{u}$ are the currents in the coils.

By the first order optimality conditions we know that for solutions $(\mathbf{u}^*, \mathbf{y}^*)$ of (14) there exist so called adjoint states $\mathbf{p}^*$ of the same dimension as $\mathbf{y}^*$ such that

$$\begin{aligned} K_{\mathbf{y}}^T(\mathbf{y}^*) + \mathbf{B}_{\mathbf{y}}^T(\mathbf{y}^*, \mathbf{u}^*)\mathbf{p}^* &= 0, \\ R_{\mathbf{u}}^T(\mathbf{u}^*) + \mathbf{B}_{\mathbf{u}}^T(\mathbf{y}^*, \mathbf{u}^*)\mathbf{p}^* &= 0, \\ \mathbf{B}(\mathbf{y}^*, \mathbf{u}^*) &= 0. \end{aligned} \tag{15}$$

Here the subscripts $_{\mathbf{y}}$ and $_{\mathbf{u}}$ denote differentiation with respect to $\mathbf{y}$ and $\mathbf{u}$, respectively. A Newton-type method for solving (15) are iterations of the type

$$\begin{pmatrix} K_{\mathbf{yy}}(\mathbf{y}^k) & 0 & \mathbf{B}_{\mathbf{y}}^T(\mathbf{y}^k, \mathbf{u}^k) \\ 0 & R_{\mathbf{uu}}(\mathbf{u}^k) & \mathbf{B}_{\mathbf{u}}^T(\mathbf{y}^k, \mathbf{u}^k) \\ \mathbf{B}_{\mathbf{y}}(\mathbf{y}^k, \mathbf{u}^k) & \mathbf{B}_{\mathbf{u}}(\mathbf{y}^k, \mathbf{u}^k) & 0 \end{pmatrix} \begin{pmatrix} \mathbf{y}^{k+1} - \mathbf{y}^k \\ \mathbf{u}^{k+1} - \mathbf{u}^k \\ \mathbf{p}^{k+1} \end{pmatrix} = - \begin{pmatrix} K_{\mathbf{y}}^T(\mathbf{y}^k) \\ R_{\mathbf{u}}^T(\mathbf{u}^k) \\ \mathbf{B}(\mathbf{y}^k, \mathbf{u}^k) \end{pmatrix}. \tag{16}$$

The iteration scheme (16) is different from Newtons method for (15), since it neglects second order derivatives of $\mathbf{B}(\mathbf{y}, \mathbf{u})$. It is known that such modifications are prone to convergence issues, but this doesn't seem to be an issue for our specific application. In the terminology of Newton methods we use rather a *quasi* Newton method, than an *exact* Newton method.

Since in our case the number of currents is much smaller than the dimension of the approximation space $\mathscr{V}^{\text{ex}}$ and $\mathscr{V}^{\text{in}}$, the dimension of (16) is roughly twice as large as the dimension of non-linear discrete free-boundary equilibrium problem (12). Even though it would be possible to invert the linear system in (16) with a direct solver, we have implement an algorithm (see Algorithm (1)) based on the Schur complement, as this appears as a minor modification of Newton's method for the constraint (12). When the iteration stops, the auxiliary variable $\mathbf{Y}$ is basically the sensitivity $\mathbf{y}_{\mathbf{u}}(\mathbf{u})$. In general, it is recommended to avoid the explicit calculation of theses sensitivities and adjoint methods were introduced for exactly that purpose. However, in our case, with very few number of control parameters, this is not an issue.

The iteration scheme (16) for the constraint optimization problem (14) involves first order derivatives of $\mathbf{B}(\mathbf{y}, \mathbf{u})$ and first and second order derivatives of $R(\mathbf{u})$ and $K(\mathbf{y})$. But as we have explicit expression for $\mathbf{B}(\mathbf{y}, \mathbf{u})$, $R(\mathbf{u})$ and $K(\mathbf{y})$ that are algebraic in $\mathbf{u}$ and $\mathbf{y}$ we can also provide the required derivatives.

Algorithm 1 quasi SQP as modification (magenta) of Newtons method for the constraints

$\Delta\mathbf{y} \leftarrow 1$, $\mathbf{y} \leftarrow \mathbf{y}^0$, $\Delta\mathbf{u} \leftarrow 1$, $\mathbf{u} \leftarrow \mathbf{u}^0$
while $\|\Delta\mathbf{y}\| > 0$, $\|\Delta\mathbf{u}\| > 0$ **do**
  $(\Delta\mathbf{y}, \mathbf{Y}) \leftarrow -(\mathbf{B}_{\mathbf{y}}(\mathbf{y}, \mathbf{u}))^{-1}(\mathbf{B}(\mathbf{y}, \mathbf{u}), \mathbf{B}_{\mathbf{u}}(\mathbf{y}, \mathbf{u}))$
  $\mathbf{m} \leftarrow R_{\mathbf{u}}^T(\mathbf{u}) + \mathbf{Y}^T K_{\mathbf{y}}^T(\mathbf{y}) + \mathbf{Y}^T K_{\mathbf{yy}}(\mathbf{y})\Delta\mathbf{y}$
  $\mathbf{M} \leftarrow R_{\mathbf{uu}}(\mathbf{u}) + \mathbf{Y}^T K_{\mathbf{yy}}(\mathbf{y})\mathbf{Y}$
  $\Delta\mathbf{u} \leftarrow -\mathbf{M}^{-1}\mathbf{m}$
  $\mathbf{y} \leftarrow \mathbf{y} + \Delta\mathbf{y} + \mathbf{Y}\Delta\mathbf{u}$
  $\mathbf{u} \leftarrow \mathbf{u} + \Delta\mathbf{u}$
end while

3.5 A Case Study

We present a first case study for the tomamak CFETR. The machine CFETR, the China Fusion Engineering Test Reactor, is a planed device in the roadmap for the realization of

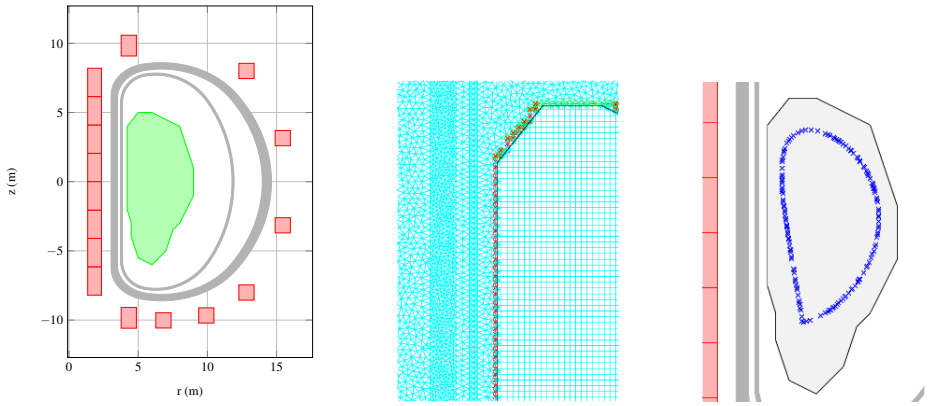

Fig. 10 CFETR: the geometry (left), a zoom of the composite meshes (center), and the location the points $\mathbf{x}_i$ in the definition of the objective functional K_1 (right).

fusion energy in China, that will follow ITER. The geometry of the machine is sketched in Figure 10. All the following caclulations are based on the MEM-M discretization (12) of the free-boundary equilibrium problem (7). We use lowest order Lagrangian finite element for $\mathscr{V}^{\mathrm{ex}}$ and the Bogner-Fox-Schmit finite element for $\mathscr{V}^{\mathrm{in}}$. In order to create snowflake-like configurations similar to the ones for HL-2M in Figure 9 we introduce two objective functionals:

$$\begin{aligned} K_1(\psi) &= \sum_{i=2}^{N_{\mathrm{desi}}} \big(\psi(\mathbf{x}_i) - \psi(\mathbf{x}_1)\big)^2 \\ K_2(\psi) &= \|\nabla\psi(\mathbf{x}_0)\|^2 . \end{aligned} \tag{17}$$

The objective functional K_1 forces ψ to be constant on the prescribed points $\mathbf{x}_1, \dots \mathbf{x}_{N_{\mathrm{desi}}}$. The objective functional K_2 forces ψ to have a stationary point at $\mathbf{x}_0$. Using K_1 alone for the formulation of the optimal control problem (14), is the standard approach to find a certain configuration of plasma currents that give an equilibrium boundary that is close to the prescribed points $\mathbf{x}_i$.

In the following we set $\mathbf{x}_0 = (5.42, -4.62)$ and the solve optimal control problems (14) with the objective functional

$$K(w;\psi) = K_1(\psi) + wK_2(\psi)$$

for changing values of w. In Figure 11 we see that for a sufficiently large value of w our approach is capable to create snowflake-like plasma equilibrium configurations. Moreover, it is easily possible, to find configurations for a great variety of locations of the lower stationary point.

References

1. Achdou, Y., Maday, Y.: The mortar element method with overlapping subdomains. SIAM J. Numer. Anal., **40(2)**, 601–628 (2002)
2. Albanese, R., Blum, J., De Barbieri, O.: On the solution of the magnetic flux equation in an infinite domain. In *EPS. 8th Europhysics Conference on Computing in Plasma Physics*, 41–44 (1986)
3. Blum, J., Le Foll, J., Thooris, B.: The self-consistent equilibrium and diffusion code SCED. Computer Physics Communications, **24**, 235–254 (1981).

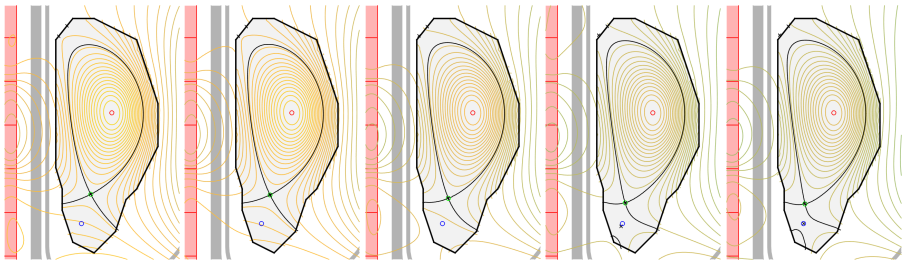

Fig. 11 The solutions of the optimal control problem with objective functional $K(w;\psi) = K_1(\psi) + wK_2(\psi)$ and $w = 0, 1, 10, 100, 1000$ (from left to right), $\mathbf{x}_0$ is indicated by the blue circle.

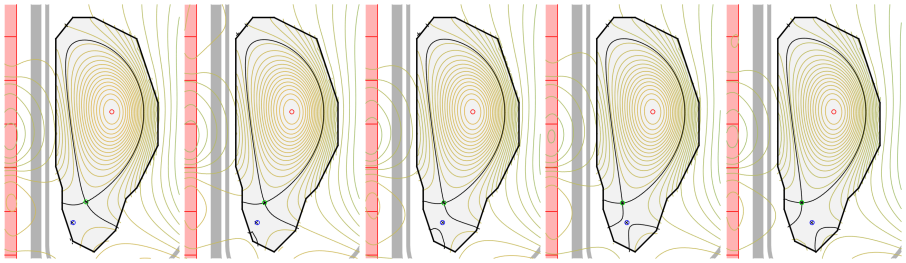

Fig. 12 The solutions of the optimal control problem with objective functional $K(w;\psi) = K_1(\psi) + 1000K_2(\psi)$ and $\mathbf{x}_0$ is indicated by the blue circle.

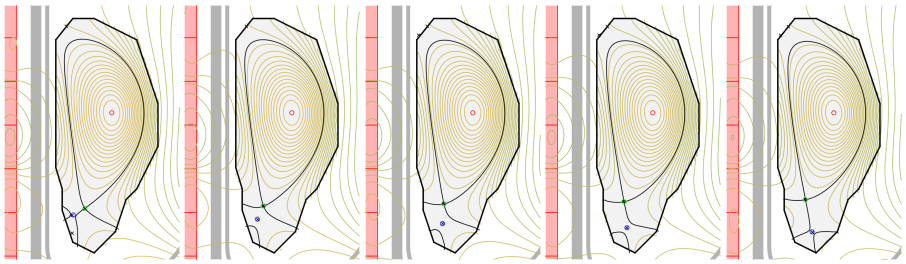

Fig. 13 The solutions of the optimal control problem with objective functional $K(w;\psi) = K_1(\psi) + 1000K_2(\psi)$ and $\mathbf{x}_0$ is indicated by the blue circle.

4. Blum, J.: Numerical Simulation and Optimal Control in Plasma Physics. Wiley/Gauthier-Villars Series in Modern Applied Mathematics, (1989)
5. Cai, X.-C., Dryja, M., Sarkis M.: Overlapping nonmatching grid mortar element methods for elliptic problems. SIAM J. Numer. Anal., **36(2)**, 581–606 (1999)
6. Chesshire, G., Henshaw, W.D.: Composite overlapping meshes for the solution of partial differential equations. J. Comput. Phys., **90(1)**, 1–64 (1990)
7. Christophe, A., Santandrea, L., Rapetti, F., Krebs, G., Le Bihan, Y.: An overlapping non-matching grid mortar element method for Maxwell's equations. IEEE Trans. Magn., **50(2)**, 409–412 (2014)
8. Christophe, A., Le Bihan, Y., Rapetti, F.: A mortar element approach on overlapping non-nested grids: application to eddy current non-destructive testing. Appl. Math. Comp., **267**, 71–82 (2015)
9. Faugeras, B., Heumann, H.: FEM-BEM coupling methods for Tokamak plasma axisymmetric free-boundary equilibrium computations in unbounded domains. Journal of Computational Physics, **343**, 201–216 (2017)
10. Fish, J., Belytschko, T.: Elements with embedded localization zones for large deformation problems. Comput. & Struct., **30(1)**, 247–256 (1988)
11. Freidberg, J. P.: *Ideal Magnetohydrodynamics*. Plenum US, 1987

12. Goedbloed, J.-P., Poedts, S.: *Principles of magnetohydrodynamics: with applications to laboratory and astrophysical plasmas*. Cambridge university press, 2004
13. Goedbloed, J.-P., Keppens, R., Poedts, S.: *Advanced magnetohydrodynamics: with applications to laboratory and astrophysical plasmas*. Cambridge University Press, 2010
14. Grad, H., Rubin, H.: Hydromagnetic equilibria and force-free fields. *Proceedings of the 2nd UN Conf. on the Peaceful Uses of Atomic Energy*, 190–197 (1958)
15. Grandgirard, V.: *Modélisation de l'équilibre d'un plasma de tokamak*. PhD thesis, Université de Franche-Comté, 1999.
16. Hecht., F., Lozinski. A., Pironneau. O.: Numerical zoom and the Schwarz algorithm. In Domain decomposition methods in science and engineering XVIII, Springer-Verlag, 63–73 (2009)
17. Heumann, H., Rapetti, F.: A finite element method with overlapping meshes for free-boundary axisymmetric plasma equilibria in realistic geometries. Journal of Computational Physics, **334**, 522–540 (2017)
18. Heumann, H., Blum, J., Boulbe, C., Faugeras, B., Selig, G., Ané, J.-M., Brémond, S., Grandgirard, V., Hertout, P., Nardon, E.: Quasi-static free-boundary equilibrium of toroidal plasma with CEDRES++: Computational methods and applications. *J. Plasma Phys.*, **81(6)**, 1–35 (2015)
19. Jardin, S.-C.: *Computational methods in plasma physics*. Boca Raton, FL : CRC Press/Taylor & Francis, 2010.
20. Kuznetsov,Y. A.: Overlapping domain decomposition with non-matching grids. In Recent developments in domain decomposition methods and flow problems, volume 11 of GAKUTO Int. Ser. Math. Sci. Appl., 62–71. Gakkōtosho, Tokyo (1998)
21. Lozinski, A., Pironneau, O.: Numerical zoom for advection diffusion problems with localized multiscales. Numer. Meth. PDEs, **27(1)**, 197–207 (2011)
22. Lüst, R., Schlüter, A.: Axialsymmetrische magnetohydrodynamische Gleichgewichtskonfigurationen. *Z. Naturforsch. A*, **12**, 850–854 (1957)
23. Luxon, J.-L., Brown, B. B.: Magnetic analysis of non-circular cross-section tokamaks. *Nuclear Fusion*, **22(6)**, 813–821 (1982)
24. Mote, C. D. Jr.: Global-local finite element. Int. J. Numer. Meth. Engrg., **3**, 565–574 (1971)
25. Moret, J.-M., Duval, B., Le, H., Coda, S., Felici, F., Reimerdes, H.: Tokamak equilibrium reconstruction code LIUQE and its real time implementation. *Fusion Engineering and Design*, **91**, 1–15 (2015).
26. Parter, S. V.: On the overlapping grid method for elliptic boundary value problems. *SIAM J. Numer. Anal.*, **36(3)**, 819–852 (1999)
27. Ryutov, D. D.: Geometrical properties of a snowflake divertor. *Physics of Plasmas*, **14(6)**, 064502 (2007)
28. Ryutov, D. D., Cohen, R. H., Rognlien, T. D., Umansky, M. V.: The magnetic field structure of a snowflake divertor. *Physics of Plasmas*, **15(9)**, 092501 (2007)
29. Steger, J. L., Benek, J. A.: On the use of composite grid schemes in computational aerodynamics. *Comput. Methods Appl. Mech. Engrg.*, **64**, 301–320, (1987)
30. Shafranov, V. D.: On magnetohydrodynamical equilibrium configurations. *Soviet Journal of Experimental and Theoretical Physics*, 6:545, 1958.
31. M. D. Truong. The mortar element method for the free-boundary toroidal plasma equilibrium problem. Master's thesis, Erasmus Mundus Joint Master Degree in Mathematical Modeling in Engineering MATHMODS, 2016.
32. Wesson, J.: *Tokamaks*. The International Series of Monographs in Physics. Oxford University Press, 2004.

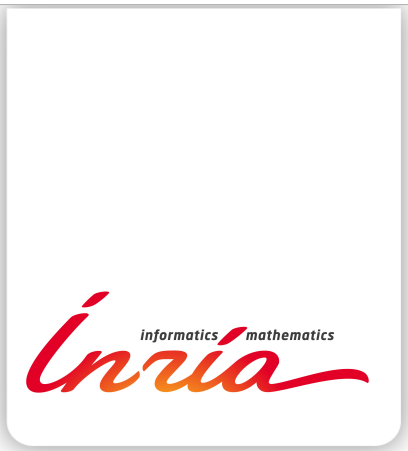

RESEARCH CENTRE
SOPHIA ANTIPOLIS – MÉDITERRANÉE

2004 route des Lucioles - BP 93
06902 Sophia Antipolis Cedex

Publisher
Inria
Domaine de Voluceau - Rocquencourt
BP 105 - 78153 Le Chesnay Cedex
inria.fr

ISSN 0249-6399